sustainability

MDPI

Article

Modeling Tetracycline Adsorption onto Blast Furnace Slag Using Statistical and Machine Learning Approaches

Harsha S. Rangappa [1,2], Phyu Phyu Mon [3], Indika Herath [4], Giridhar Madras [5], Chuxia Lin [2] and Challapalli Subrahmanyam [1,3,*]

[1] Center for Interdisciplinary Programs, Indian Institute of Technology Hyderabad, Kandi, Sangareddy 502285, India
[2] Centre for Regional and Rural Futures, Faculty of Science, Engineering and Built Environment, Deakin University, Burwood, VIC 3125, Australia
[3] Department of Chemistry, Indian Institute of Technology Hyderabad, Kandi, Sangareddy 502285, India
[4] Centre for Regional and Rural Futures, Faculty of Science, Engineering and Built Environment, Deakin University, Waurn Ponds, VIC 3216, Australia
[5] Department of Chemical Engineering, Indian Institute of Technology Hyderabad, Kandi, Sangareddy 502285, India
* Correspondence: csubbu@iith.ac.in

Abstract: Ground granulated blast furnace slag (GGBS) is a primary industrial waste product of iron production, and its improper disposal has been a serious environmental problem. This study aims to modify the GGBS using oxalic acid (GGBS-Ox) for the adsorption of tetracycline (TC) from an aqueous solution. GGBS-Ox was synthesized and characterized via FTIR, XRD SEM, XPS, BET, and DLS. The effects of process parameters, involving initial solution pH, stirring speed, and contact time, are evaluated by utilizing response surface methodology (RSM), artificial neural network (ANN), and random forest (RF) based models. The experimental results indicate that the removal efficiency of TC is significantly affected by the initial pH of the solution. The RSM, ANN, and RF models accurately simulated the experimental data, as indicated by the high coefficient of determination (R^2), which was 0.98, 0.95, and 0.98, respectively. Additionally, kinetics, isotherm, and thermodynamic models were evaluated for the adsorption of TC onto GGBS-Ox. The findings of this study demonstrated the utilization of GGBS-Ox as an efficient and sustainable adsorbent for the treatment of TC and can be considered as a potential adsorbent for wastewater treatment.

Keywords: pharmaceutical pollution; Box–Behnken design; emerging contaminates; industrial waste-based adsorbents; economical adsorbent; circular economy

Citation: Rangappa, H.S.; Mon, P.P.; Herath, I.; Madras, G.; Lin, C.; Subrahmanyam, C. Modeling Tetracycline Adsorption onto Blast Furnace Slag Using Statistical and Machine Learning Approaches. *Sustainability* **2024**, *16*, 464. https://doi.org/10.3390/su16010464

Academic Editor: Antonio Zuorro

Received: 20 November 2023
Revised: 22 December 2023
Accepted: 29 December 2023
Published: 4 January 2024

1. Introduction

Tetracycline (TC) is one of the most widely used antibiotics for treating different bacterial infections in humans and animals [1]. However, excessive usage of TC causes antibiotic-resistant pathogens to emerge, leading to profound environmental and health implications when discharged into aquatic systems. Tetracyclines have been categorized as one of the emerging pollutants because of their occurrence in aquatic ecosystems [2]. Due to growing concerns over increased TC and other antibiotic concentrations in wastewater, removing them from wastewater before disposal is creating a greater challenge. Raw domestic and industrial wastewater often contains TC concentrations varying from 100 ppb to 20 ppm [3,4]. Therefore, it is essential to establish a cost-effective and efficient approach for removing antibiotics before discharging wastewater into aquatic habitats. Traditional sewage treatment plants are found to be inadequate to treat the pharmaceuticals in aquatic ecosystems [5]. Hence, various advanced wastewater treatment, methods such as chemical decomposition, biological treatment, photocatalysis, electrochemical oxidation, ozonation, advanced oxidation [6], and adsorption [7,8], have emerged. Adsorption is one of

the most widely used methods due to its simplicity and affordability. Numerous studies have explored the efficacy of biochar, carbon nanotubes, zeolites, activated carbon, and clay minerals in the adsorption of diverse contaminants, including pharmaceutical compounds [9]. However, these adsorbents are expensive and face availability issues for large-scale applications. In order to address this issue, waste products from agriculture [10] and industry [7] are being used as substitutes for conventional adsorbents to it more feasible for the adsorption process to eliminate diverse pollutants in water and wastewater [11,12].

GGBS is a major byproduct of iron production that is primarily used in the construction industry [13], and a significant portion of it ends up as environmental waste [14]. GGBS primarily consists of calcium, silicon, iron, aluminum, and manganese oxides [15]. GGBS has been effectively applied for the removal of numerous contaminants, such as dye, heavy metal ions, and a few emerging contaminants, because of its ion-exchange capacity and alkalinity [16,17]. Further, its availability, cost-effectiveness, lack of toxicity, and ease of modification make it a desirable adsorbent. GGBS is also employed for the remediation of diverse organic contaminants within an aqueous milieu, including ECs [18–20]. Gupta et al. (2006) studied the use of raw steel slag waste to remove 2,4-dichloro phenoxyaceticacid (2,4-D) [18]. The findings indicated that the utilization of raw steel slag as an adsorbent is not efficacious, due to its lower surface area. Bhuyan et al. (2022) examined the alkaline activation of blast furnace slag for the removal of methylene blue (MB) [19]. It had a surface area of 83 m^2/g after alkaline treatment, giving it a removal efficiency of 74% at 5 ppm concentration of MB. Saood et al. (2022) compared two different steel factory slags and tested them for the removal of Eriochrome black T (EBT) [16]. It was shown that the slags had a good affinity for the EBT dye, with an adsorption capacity of 100% for a dye concentration of 20 ppm at pH 2. Further, Zubair et al. (2022) examined the synthesis of a biochar-steel dust composite for treating phosphate [21]. The adsorption capacity of the composite material was 175 mg/g at pH 4 for 100 ppm phosphate. The important role that steel dust plays in the adsorption process has been clearly shown in these studies. This suggests that steel slag could be a good adsorbent for effectively cleaning up pollutants in water [21]. Therefore, the utilization of GGBS can be regarded as an effective strategy for promoting and attaining a circular economy [22]. This is primarily attributed to its ability to offer alternative applications or pathways within the life cycle of this industrial waste source. By doing so, GGBS aids in waste reduction and contributes to the advancement of sustainable development. This is achieved through the process of modification, which involves enhancing the value of waste materials, as well as the significant enhancement of surface area and porosity through the upcycling process. GGBS may be seen as offering further benefits to waste materials that would otherwise pose challenges, facilitating their transformation into more valuable resources [23].

Over the last decade, various statistical and machine learning-based prediction models have emerged to evaluate the effects of process parameters on the objective function for process optimization. Response Surface Methodology (RSM) based on rotatability is one of the most popular classical statistical tools among researchers for studying the second-order interaction effects and evaluating individual parameter effects on the process. The CCD and BBD are commonly utilized techniques in RSM [24]. Traditional optimization approaches need a higher number of runs and are time-demanding, but RSM has the ability to predict process parameters in a limited number of runs while employing minimal resources [24,25]. BBD-based RSM models facilitate optimal settings and provide better accuracy with a smaller number of runs. For large-scale optimization, machine learning approaches such as artificial neural network (ANN) and random forest (RF) have been increasingly adopted by researchers. The utilization of ANN and RF represents an advanced and robust approach to efficient predictions. ANN possesses the ability to autonomously learn and operate even with inadequate information and spread data over the complete network. The ANN can also predict experimental variations in a wide range of applications [26]. Traditional techniques of regression and classification may be improved by RF combining hundreds of decision trees. RF can identify correlations between variables in a small dataset as well

as offering regular observation of processes and tolerance for many input variables [27]. Elijah et al., (2021) carried out a study in which ANN and RF were employed to explore the adsorption of EBT dye using a modified clay [28]. Geyikc, (2012) constructed models in the form of RSM and ANN to examine the effectiveness of red mud as an adsorbent for extracting lead that has leached from industrial waste [29]. Ahmadi Azqhandi et al. (2017) investigated the modeling of RBF-NN, RF, and RSM to study the adsorption of Brilliant Green on ZnS-NP-AC adsorbent [30]. Their findings suggested RF as the most appropriate model to determine the adsorption capacity. The results demonstrated that these models offered high accuracy in predicting the adsorption capacity. Hence, these models prove to be efficient for optimizing the process parameters in the adsorption process.

In recent years, Oxalate-based adsorbents have been applied to treat a wide variety of waterborne contaminants. They are immensely beneficial due to their biodegradability, cost-effectiveness, non-toxicity, and global availability [31]. These adsorbents are extensively employed for the treatment of various metal ions, including nickel, cobalt, lead, and zinc, from aqueous environments and industrial effluents [32]. The oxalate-treated slag has been utilized for treating lead (Pb), cadmium (Cd), and cobalt (Co) [32,33]. However, to the best of the author's knowledge, there have been no studies on the utilization of oxalate-treated GGBS for the removal of any organic contaminants. Moreover, it is worth noting that the modeling and comparison of TC adsorption parameters using RSM, ANN, and RF techniques are yet to be explored. Therefore, this study focuses on the synthesis of oxalate modified GGBS for the removal of TC and characterizing the adsorbent via FTIR, XRD SEM, XPS, BET, and DLS. Further, the mutual and individual effects of adsorption parameters, such as initial solution pH, stirring speed, and contact time, on the removal efficiency of TC are determined by deploying BBD-based RSM, ANN, and RF models. This study also investigates the kinetics and isotherm models along with thermodynamics to evaluate the adsorption mechanism involved in TC removal. In summary, this study would yield valuable and meaningful contributions to the broader academic community working on non-conventional adsorbents for treating different aquatic pollutants.

2. Materials and Methods

2.1. Chemicals

The oxalic acid, sodium hydroxide, sodium hydroxide (NaOH), tetracycline hydrochloride, Hydrochloric acid (HCl) and Ground granulated blast furnace slag (GGBS) are procured from Fisher Scientific, FINAR Limited, Alfa Aesar chemicals, and Nature and Greens Pvt. Ltd. (Jamnagar, India). All experimental investigations are conducted using Millipore water.

2.2. Preparation of Adsorbent

A total of 5 g of GGBS powder was dissolved in 40 mL of a 1 M oxalic acid solution. The resulting mixture underwent stirring for 90 min. Subsequently, 10 mL of a 3 M NaOH solution was added dropwise to the mixture, which continued to be stirred on a hot plate set to 80 °C. Once a brown precipitate emergence was observed, the precipitate was then put into a water bath maintained at 80 °C and allowed to undergo crystallization for 12 h, promoting improved crystalline structure. Then, the resulting precipitate was subjected to vacuum filtration, then rinsed with deionized water until a neutral pH of 7 was attained. The washed precipitate was then dried overnight in an oven operating at 80 °C. After drying completely, the powder was kept in an airtight vial until it was needed for adsorption studies [32,33].

2.3. Characterization Details

Analysis of XRD was conducted to determine the crystal phase of the adsorbents using a PANalytical X'pert PRO X-ray diffractometer. The measurements were conducted utilizing a copper K-alpha (k = 1.541) source, employing a nickel filter. The scanning procedure was carried out within the angular range of 5–80°, with a step size of 0.0167°

and a scan rate of 0.0301°/s. To characterize the surface of the adsorbent, a JIB-4700 F FE-SEM instrument manufactured by JEOL, Akishima, Japan, was utilized for SEM. FTIR spectroscopy employing an FTIR-Bruker a-T model was employed within the spectral range of 4000 to 500 cm^{-1}. The determination of the specific surface area (SSA) of the adsorbents was carried out using the BET (Brunauer, Emmett, and Teller) method, employing a Quantachrome Nova 2200 (Boynton Beach, FL, USA) surface area analyzer. The adsorption and desorption isotherms were obtained by degassing the samples at 150 °C for three hours prior to analysis. The XPS analysis of the synthesized adsorbents was conducted using a Krato axis Ultra Spectrometer manufactured by Shimadzu Corporation (Kyoto, Japan). The measurements were performed using an Al-K source operating at an energy level of 1489.5 eV, with an emission current of 10 mA and an emission voltage of 15 kilovolts (kV). The concentration of TC was measured using a PG Instruments Ltd. (Lutterworth, UK), India T90 + UV-vis spectrometer. To determine the PZC and particle size, a Nanotrac wave II DLS analyzer was used in conjunction with water measurements at 26 °C. Before measuring the zeta potential, the POC was determined by modulating the pH of the solution from 2 to 12 with NaOH and HCl while stirring continuously for 12 h.

2.4. Batch Experiment Details

This study aimed to examine the adsorption of TC on GGBS-Ox through a series of batch experiments. All experiments involved 50 mL of aqueous TC solution at 25 ± 3 °C. Experiments were performed to assess the optimal dosage of adsorbent between 10 mg and 100 mg, as well as the optimal concentration of TC between 20 ppm and 100 ppm, and the contact time was 180 min. Following each adsorption experiment, 1 mL of samples were subjected to filtration and subsequent centrifugation at a speed of 6000 revolutions per minute for 10 min, until complete settling of adsorbent was achieved. A UV-visible spectrophotometer operating at a specified wavelength of 358 nm was used to determine the concentration of TC. The pH of the solution was adjusted with NaOH or HCl solution (0.1 M). All experiments are performed three times, and the average of the results is used in these analyses. The error in percent removal obtained was less than ±2% in all cases. Additionally, the removal efficacy of TC for BBD was established through three repeated trials conducted under ideal conditions. The efficiency of TC removal (%) and the adsorption capacity of TC was determined using the following equations:

$$Removal\ efficiency(\%) = \frac{C_o - C_t}{C_o} \times 100 \quad (1)$$

$$Qe = \frac{(C_o - C_t) \times V}{W} \quad (2)$$

In the above equations, C_o denotes the initial concentration of TC (ppm), while C_t signifies the TC concentration at a particular time. Q_e represents the adsorption capacity (mg/g), V corresponds to the volume of the solution (L), and W denotes the mass of the adsorbent (g).

2.5. Response Surface Methodology

The RSM-based BBD reveals the extent of the correlation between the selected adsorption parameters. The primary objective of this investigation is to model the adsorption of TC from an aqueous solution into GGBS-Ox. The Design-Expert software, version 11, was utilized. Based on the preliminary experiment, the BBD experiment is conducted using independent adsorption factors, such as (A) pH, (B) contact time, and (C) stirring speed, with percent removal efficiency as the response (Y). Each independent parameter was subdivided into three levels (−1, 0, and 1), allowing the model creation of an experimental design with 17 investigative runs and five replications at the central level, as shown in

Table 1. The following is a second-order quadratic model that establishes the correlation between specific input factors and the performance of TC adsorption.

$$Y(\%) = \beta_o + \sum_{i=1}^{3} \beta_i X_i + \sum_{i=1}^{3} \beta_{ii} X_i^2 + \sum_{i>j} \beta_{ij} X_i X_j \quad (3)$$

where Y is the efficiency of TC adsorption, X_i denotes the variables under consideration, and (β_0, β_i, β_{ii}, and β_{ij}) denote the model terms, which represent the intercept, quadratic, linear, and interaction effects, respectively. Analysis of variance (ANOVA) was performed to determine the relevance and adequacy of the postulated model using the Design-Expert program. The multiple regression parameters were calculated, such as the coefficient of determination R^2, adjusted R^2, *p*-value, and lack-of-fit.

Table 1. Levels of parameters for BBD experiments.

Independent Parameters	Coded and Uncoded Values		
	−1	**0**	**+1**
Initial pH	2	7	12
Contact time (min)	10	50	90
Stirring speed (rpm)	100	300	500

2.6. Artificial Neural Network

An ANN is a computational model that draws inspiration from the structure and functioning of the human brain and nervous system. To identify non-linear relationships between variables that cannot be stated mathematically, ANN is a trustworthy and reliable validation methodology [34]. ANN consists of several interconnected neurons that flow as shown in Figure S1a. The precise number of neurons can be determined through an iterative process. In this study, the data obtained from BBD and other experiments are used to train and test the ANN modal. The input data consists of initial pH, time (min), and stirring speed, with the output variable as removal (%). The data set is divided into training (75%) and testing data (25%) set for modal input [35]. In this case, three hidden layers are considered, with 15 neurons in each layer. The model uses the Kernel initializer as normal in the hidden and output layers. The rectified linear activation function (ReLU) and linear activation function are employed in hidden and output layers, respectively.

2.7. Random Forest

RF is a combination of the regression trees method and a large set of classifications. RF takes data samples from the input data and constructs a decision tree, followed by a voting procedure for each predicted parameter and a determination of the highest-voted predicted result, as shown in Figure S1b [36]. In this study, the data obtained from BBD and preliminary experiments on the RF model are trained and tested. The data set is divided into training (70%) and testing data (30%) for modal input. The model consists of 15 trees taken after an iterative process. The inputs consist of the initial pH, contact time (min), and stirring speed (rpm). The output is the removal (%).

3. Results and Discussion

3.1. Adsorbent Characteristics

The XRD spectra for GGBS and GGBS-Ox are shown in Figure 1a. The raw GGBS shows an amorphous phase of Akemanite ($Ca_2Mg(Si_2O_7)$), Gehlenite ($Ca_2Al(AlSi)O_7$, and Merwinite ($Ca_3Mg(SiO_4)$) [32,37]. Oxalic acid treatment of GGBS produced higher intensity peaks. The oxalate treatment forms different oxalate ligands ($C_2O_4{}^{-2}$), and the presence of NaOH helps in the nucleation of these crystals. Calcium aluminum silicate hydrate crystals were recognized by the low-intensity peaks at 30.94° and 45.8° (ICCD 01 087 0582).

Whereas the peaks at 14.86°, 24.48°, and 30.18° were found to match the (001), (020), and (002) crystalline planes of calcium oxide monohydrate, respectively (ICDD 98 024 6802) [32].

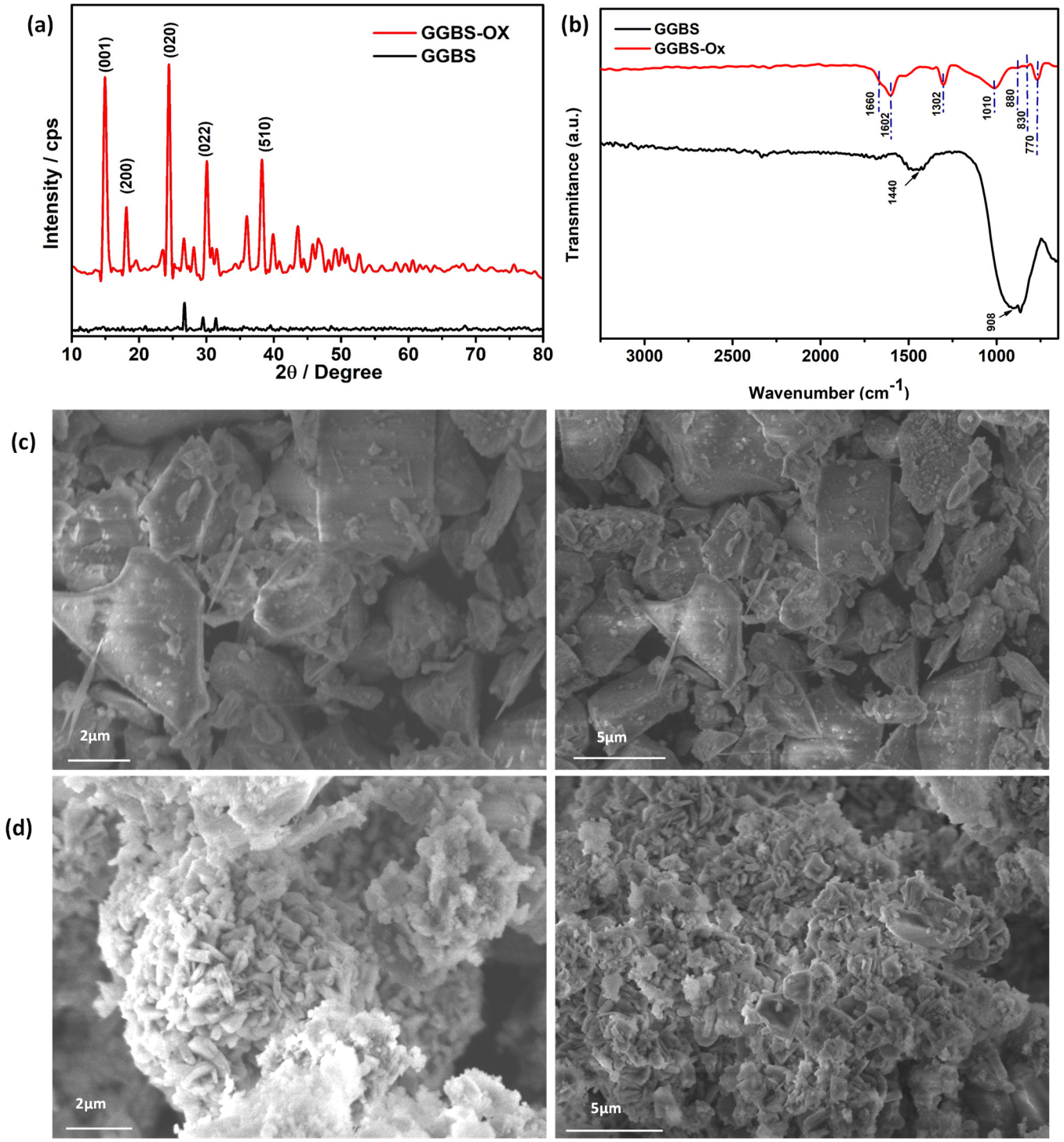

Figure 1. (**a**) XRD pattern of GGBS and GGBS-Ox (**b**) FTIR of GGBS and GGBS−Ox; SEM image of (**c**) GGBS and (**d**) GGBS−Ox.

The FTIR spectra of the GGBS and GGBS-OX are illustrated in Figure 1b. The wave number of 947 cm^{-1} represents the asymmetric stretching mode of Si-O-Al bonds. The wave number of 908 cm^{-1} is indicative of the vibrational stretching of Si-O bonds. Additionally, the peak observed between 600 to 550 cm^{-1} is indicative of the presence of Al_2O_3 in GGBS [38]. The oxalate treatment of the GGBS confirms the formation of different composite

adsorbents due to the presence of characteristic peaks at 1602 and 1302 cm^{-1} that can be attributed to Si-O-Al and Si-OH bonds respectively, while the peak 1010 cm^{-1} indicates the Si-O bond stretching. The characteristic bands between 1560 to 1360 and 880 cm^{-1} are related with carbonate CO_3^{2-} phase [39]. The presence of peaks at 770 and 830 cm^{-1} can be attributed to the stretching vibration of the C-C and C=C bonds respectively [32,40].

The specific surface areas (SSA) of GGBS and GGBS-Ox we determined using N_2 adsorption and desorption isotherms. The untreated GGBS exhibited a significantly low SSA of 5 m^2/g and GGBS-Ox displayed a notably high SSA of 133 m^2/g, which is 25 times greater than that of GGBS. The adsorption and desorption isotherm for GGBS and GGBS-Ox are illustrated in Figure S2, indicating that GGBS-Ox is a mesoporous material by exhibiting a type IV isotherm. Oxalic acid modification exhibits the capability to effectively eliminate surface impurities. Moreover, it possesses an optimal microporous and mesoporous configuration, thereby rendering it highly suitable for the intended purpose, and it also does not generate a substantial quantity of waste materials [41]. It facilitates the formation of aluminosilicate through the reaction between GGBS and an alkaline solution; further, the formation of calcium oxalate contributes to the increased surface area [32,33]. The surface area of the GGBS-Ox was reduced to 91 m^2/g after the adsorption of TC. The decrease in surface area of GGBS-Ox may be attributed to the attachment of the TC molecules to the pores. The decrease in surface area observed after the adsorption of the TC indicates that pore filling is involved in the removal mechanism [42]. The results obtained from the DLS measurements depicting the particle size distribution as well as the average particle size of both GGBS and GGBS-Ox are presented in Figure S3. The DLS analysis yielded findings indicating that the mean particle size of GGBS and GGBS-OX was approximately 2.35 µm and 2.26 µm, respectively. These results suggest that there is no significant change in particle size following the treatment.

SEM imaging was utilized to examine the transformation in the morphology of raw GGBS and GGBS-Ox. The SEM micrograph reveals the formation of a porous agglomerated flower-like structure in GGBS-Ox (Figure 1d), whereas the raw GGBS has a non-porous structure with a smooth surface (Figure 1c). XPS was employed to analyze the composition of GGBS and GGBS-Ox (Figure 2). GGBS was found to contain Si (18.7%), Al (10.5%), Ca (13.6%), and O (53%) as the main elements. Peaks corresponding to the binding energies of O 1s, Al 2p, and Si 2p were identified, with the O 1s peak at 531.3 eV matching Al_2O_3 and Si_2O_3 in GGBS. Oxalic acid treatment converted the Al_2O_3 and Si_2O_3 into AlO, SiO, and C=O, as evidenced by the XPS and FTIR data. This resulted in the formation of a good and efficient adsorbent for the adsorption of TC on this material.

3.2. Adsorption Studies

The adsorbent dosage and initial concentration are significant factors in the removal of TC. To optimize the dosage of adsorbent, a 50 mL solution containing TC with a concentration of 40 ppm was utilized, and different dosages of adsorbent, such as 10 mg, 20 mg, 50 mg, 75 mg, and 100 mg, were used. Figure 3a illustrates that there is a positive correlation between the adsorbent dosage and the removal percentage. This phenomenon may be attributed to the increased adsorbent dosage, leads to an increased number of active sites on the surface of GGBS-Ox, thereby enhancing its capacity for the adsorption of TC [16,43]. It was observed that the removal percentages at 10 mg and 20 mg were very low, and the highest removal was observed with a dosage of 100 mg. However, it was also noted that, after a dosage of 50 mg, there was no significant change in the percentage removal of TC. Therefore, 50 mg of adsorbent was taken as the optimal dosage for further studies.

The effect of initial concentration was studied over a range of concentrations including 20, 40, 50, and 100 ppm. As shown in Figure 3b, the removal percentages of TC were 68, 60, 56, and 46% for initial concentrations of 20, 40, 50, and 100 ppm of TC, respectively. The optimum concentration of TC was taken as 20 ppm in further studies. As the initial concentration of the TC increases, a corresponding decrease in the efficiency of removal

can be observed, as shown in Figure 3b. This is because the active adsorption sites become saturated, causing a reduction in the adsorption [16].

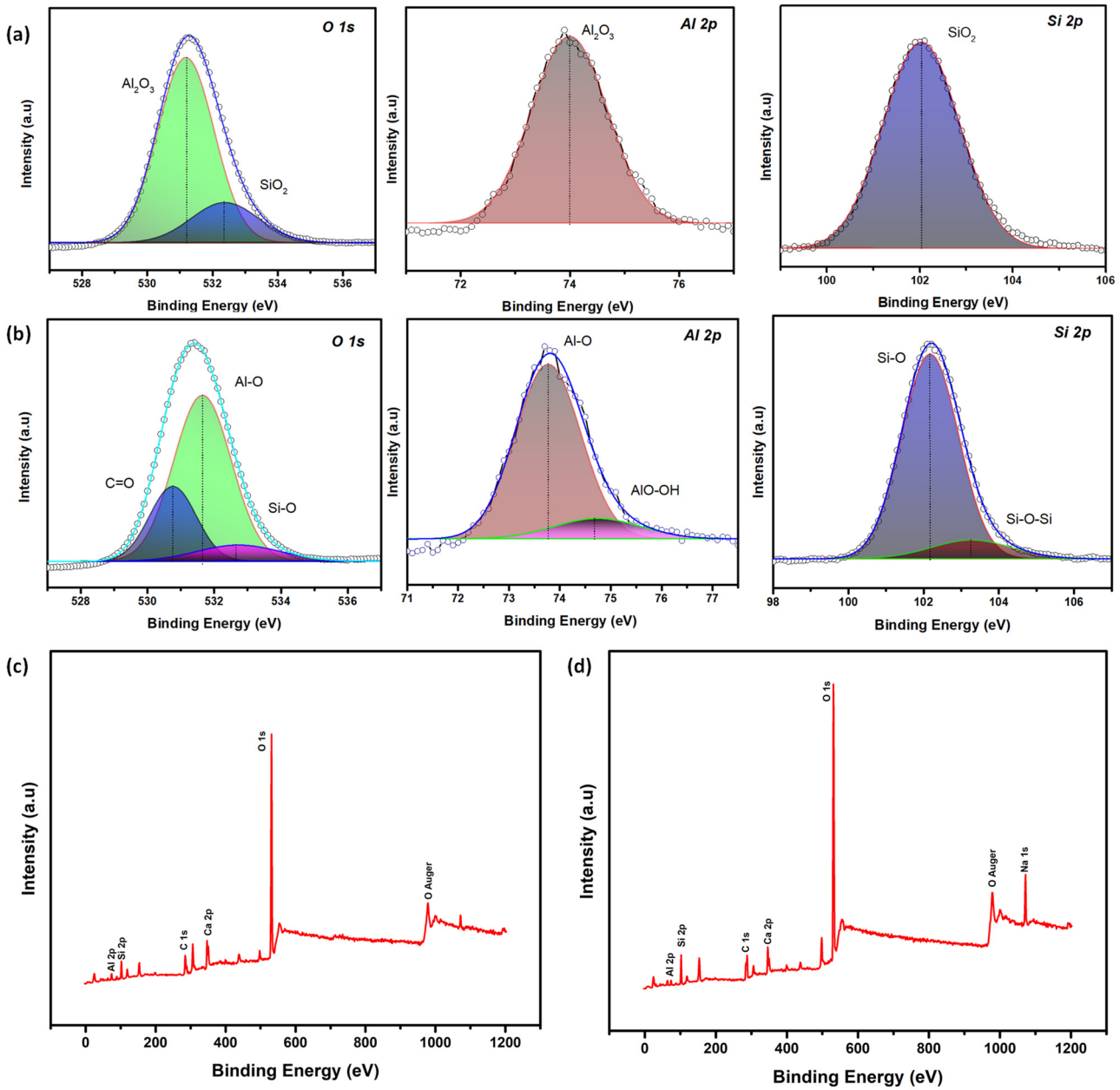

Figure 2. XPS spectra of the (**a**) GGBS O 1s, Al 2p, Si 2p (**b**) GGBS-Ox O 1s, Al 2p, Si 2p (**c**) Full spectra of GGBS (**d**) Full spectra of GGBS-Ox.

3.3. Response Surface Methodology Based Experimental Studies

The effects of selected independent parameters, such as pH, contact time, and stirring speed were evaluated for the dependent parameter of removal percent. The optimization of these parameters was performed using a BBD-based RSM. The independent and dependent variables with predicted and actual results are tabulated in Table 2. The quadratic model equation given by BBD, which shows the correlation between the dependent and independent parameters, as well as their mutual influence is presented as follows:

$$\begin{aligned} Removal\ \% = {} & 22.0320A - 0.1437 \times B - 0.0083 \times C - 1.7856 \times 10^{-16} \times AB - 7.50 \times 10^{-4} \times AC \\ & + 0.31 \times 10^{-4} \times CB - 1.2880 \times A^2 + 0.0014 \times B^2 + 0.39 \times 10^{-4} \times C^2 - 32.00575 \end{aligned} \quad (4)$$

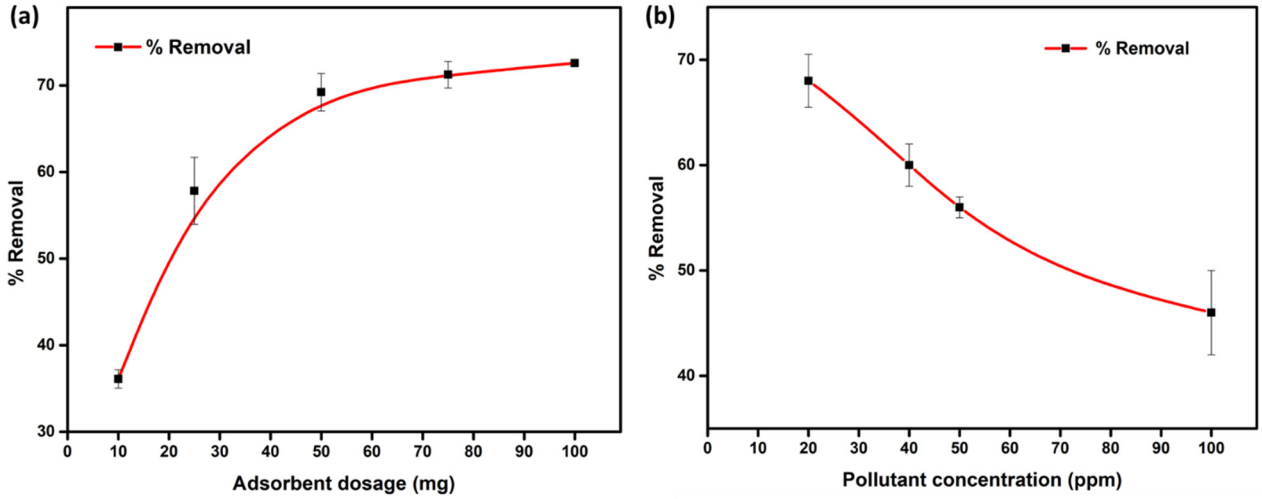

Figure 3. (**a**)The effect of adsorbent dosage on percentage removal and (**b**) the effect of pollutant concentration on the percentage removal.

Table 2. Experimental Factors and Findings in the Adsorption of TC using Box–Behnken Design.

Run	pH	Time	Stirring Speed	% Removal	
				Actual Value	Predicted Value
1	7	90	100	56	57
2	2	50	100	4	3
3	12	50	100	44	42
4	2	10	300	7	6
5	12	10	300	44	44
6	7	10	500	62	61
7	7	10	100	55	57
8	2	90	300	7	7
9	7	50	300	53	55
10	2	50	500	7	9
11	7	50	300	58	55
12	7	90	500	64	62
13	7	50	300	58	55
14	7	50	300	56	55
15	7	50	300	52	55
16	12	50	500	44	45
17	12	90	300	44	45

In the response equation, *A*, *B*, and *C* represent pH, time, and stirring speed, respectively. A positive effect of a factor implies a correlation between the increase in the factor's level and an improvement in the response. Conversely, a negative effect of the factor suggests that there is no improvement in the response as the level of the factor increases [44]. To assess the statistical significance of the model, ANOVA was utilized, as Table 3 indicates. The determined coefficient value (R^2) will explain the variation observed in the model. The model R^2 was determined to be 0.98, suggesting that approximately 2% of the overall variability remained unaccounted for by the model. Also, as shown in the table, the model is significant (p-value < 0.0001), which indicates the model fits well with experimental data. The coefficient of variation (CV), which is calculated to be 6.45%, serves as a measure of the reproducibility and reliability of the predicted model. The standard deviation (SD) (2.71) confirms that the predicted value and actual value were close. In addition, the significance of each parameter is evaluated using p-value, as Table 3 shows. Based on the model results, pH is the main parameter (p-value < 0.0001) affecting the adsorption of the TC on the GGBS-Ox surface.

Table 3. ANOVA Analysis for the Removal efficiency of TC onto GGBS-Ox.

Source	Sum of Squares	df	Mean Square	F-Value	*p*-Value	
Model	7261.49	9	806.83	109.77	<0.0001	significant
A-pH	2850.13	1	2850.13	387.77	<0.0001	
B-time	1.13	1	1.13	0.1531	0.7073	
C-stirring speed	40.50	1	40.50	5.51	0.0513	
AB	0.0000	1	0.0000	0.0000	1.0000	
AC	2.25	1	2.25	0.3061	0.5973	
BC	0.2500	1	0.2500	0.0340	0.8589	
A^2	4365.64	1	4365.64	593.96	<0.0001	
B^2	22.27	1	22.27	3.03	0.1253	
C^2	10.12	1	10.12	1.38	0.2791	
Residual	51.45	7	7.35			
Lack of Fit	20.25	3	6.75	0.8654		
Pure Error	31.20	4	7.80			
Cor Total	7312.94	16				
R^2	Adjusted R^2		Predicted R^2	Std. Dev.	Mean	C.V. %
0.9930	0.9839		0.9490	2.71	42.06	6.45

Response surface plots in three dimensions and Cantore plots were used to examine how removal percent affected the independent variables. As Figure 4a,b shows, removal percentage rapidly rises with an increase in the pH from 2 to 7. Additionally, it was observed that the highest percentage of removal of TC was achieved at a pH of 7. A decrease in the percent removal was found with further increasing the pH from 7 to 12. The minimal effect of changing time and stirring speed in the adsorption procedure implies that the reaction time has a marginal effect on the adsorption (Figure 4c). This is proven by the maximum adsorption equilibrium being reached within 10 min of the process. Figure S5 illustrates the perturbation plot, which describes the sensitivity of removal efficiency with coded independent variables.

3.4. Artificial Neural Network Modeling

The ANN was trained using a configuration consisting of three hidden layers, each containing fifteen neurons. Three different input parameters obtained from BBD and other experiments are fed into the ANN model. In order to assess the relationship between the independent variables and the dependent factor and to evaluate the ability of the ANN to make accurate predictions, performance metrics such as the root mean square error (RMSE), mean absolute error (MAE), and determination coefficient (R^2) were employed. The results show that the model achieved an R^2 value of 0.95 with different error values, as listed in Table 4. This indicates that ANN successfully models the experimental data in this study. Similar results were found in earlier studies in which ANN was capable of determining the adsorption efficiency of pollutants with a high degree of accuracy [28,29,34].

3.5. Analysis of Random Forest

The random forest network was trained with the data gathered from adsorption and BBD experiments, which were both dependent and independent. The model was loaded with the specified number of estimators and random states, which are necessary for setting the seed of the random number generator used for creating the decision trees. Performance metrics such as RMSE, MAE, and R^2 were used to measure the feasibility of the RF model and to calculate its predictability. The results of the RF model revealed a R^2 value of 0.95, which indicates that the model can predict the removal of TC appropriately; further details of the error functions are outlined in Table 4.

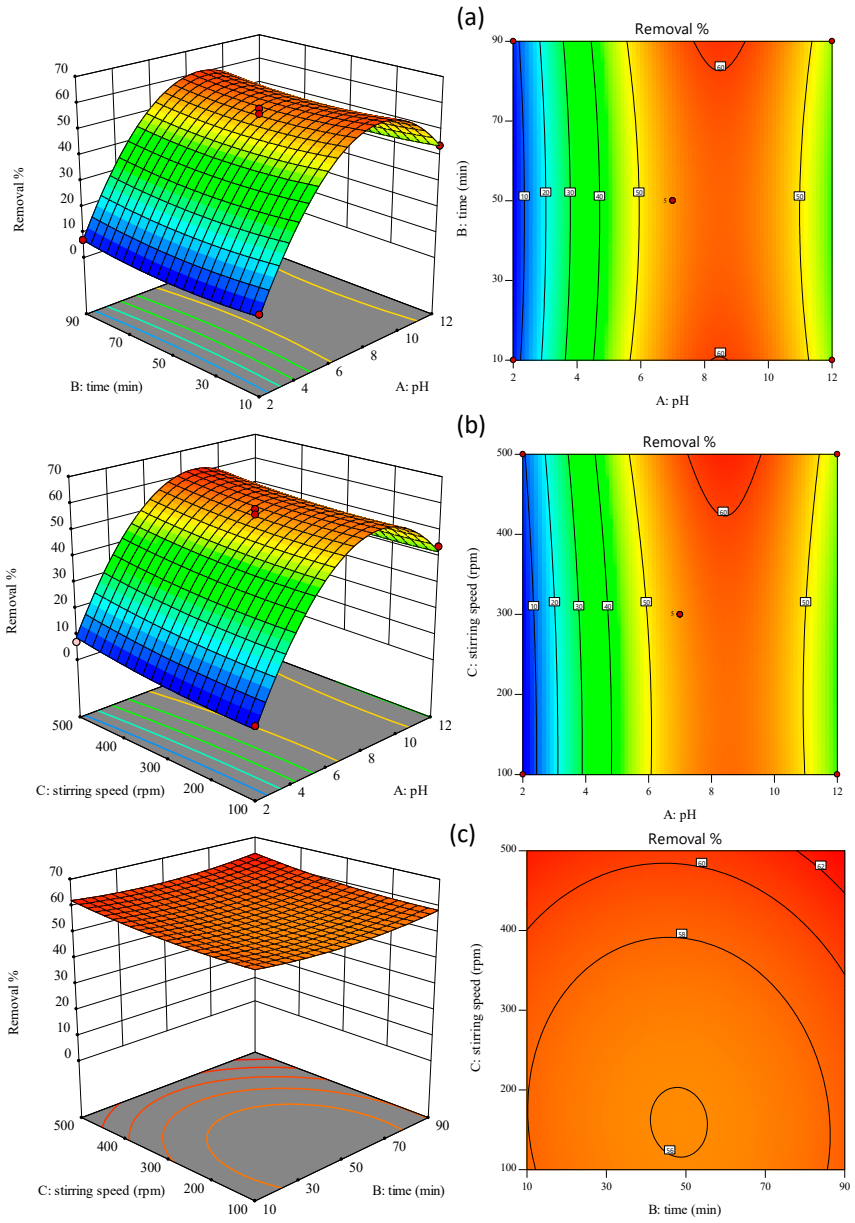

Figure 4. A 3D and 2D surface plot representation of the impact of (**a**) initial pH and Time (**b**) Stirring speed and pH, and (**c**) Stirring speed and Time on the removal efficiency (%) of TC by GGBS−Ox.

Table 4. Comparison of RSM, ANN, and RF.

	Parameter		
Model	**R^2**	**RMSE**	**MAE**
RSM	0.98	1.78	1.53
ANN	0.95	5.46	4.12
RF	0.98	3.43	2.81

3.6. Comparison of the Models

The comparison between the RSM, ANN, and RF techniques in terms of percent removal of TC was evaluated. A comprehensive evaluation was conducted by comparing the responses generated by each method with the actual observed data. BBD runs and other experimental data that fall within the BBD-independent values are used to feed ANN and

RF models. These models are evaluated statically using the *RMSE*, *MAE*, and Coefficient of Determination (R^2) using the equations given below:

$$MAE = \frac{\sum_{t=1}^{N} |X_P - X_A|}{N} \quad (5)$$

$$RMSE = \sqrt{\frac{\sum_{t=1}^{N} (X_A - X_p)^2}{N}} \quad (6)$$

$$R^2 = \frac{(\Sigma(X_A - \bar{x}_A) \times (X_P - \bar{x}_P))^2}{\left(\Sigma(X_A - \bar{x}_A)^2 \times \Sigma(X_p - \bar{x}_P)^2\right)} \quad (7)$$

The statistical comparison of the RSM, ANN, and RF models is presented in Table 5. The findings revealed a high degree of concordance between the experimental observations and the theoretical predictions made by the models, resulting in negligible residual errors. Notably, the BBD and RF models exhibited enhanced accuracy in forecasting the percentage removal of TC, as evidenced by the prevalence of statistically insignificant residual values. Moreover, Figure S4 presented a graphical representation of the strong correlation between the experimental data and the model predictions, confirming the satisfactory performance of the models. Remarkably, no substantial deviations or outliers were identified in the models' predictive capability. Since the RSM-based BBD considered the average of 3 values as an input parameter, it possesses a higher R^2 and lower error function value than that of ANN and RF. RF performed better than ANN since it uses both classification and regression. RF is an ensemble approach that aggregates the outputs from multiple decision trees to provide a more accurate prediction of the adsorption of TC into GGBS-Ox [30].

Table 5. Calculation of adsorption parameters and regression coefficients.

Kinetic Model	Initial Concentration (ppm)	Parameter		Regression Coefficient
Pseudo-first order		q_e	K_1	R^2
	20	15.95	0.027 ± 0.002	0.9208
	50	33.08	0.031 ± 0.002	0.9335
	100	53.60	0.022 ± 0.003	0.8015
Pseudo-second order		q_e	K_2	R^2
	20	15.50	0.0621 ± 0.001	0.9973
	50	32.19	0.0298 ± 0.001	0.9959
	100	50.00	0.019 ± 0.001	0.9955
Intraparticle diffusion		Ci	K_{id}	R^2
	20 (step 1)	12.17 ± 0.155	0.34 ± 0.017	0.9842
	20 (step 2)	5.35 ± 0.79	1.96 ± 0.22	0.9623
	50 (step 1)	9.55 ± 1.76	4.20 ± 0.5	0.9588
	50 (step 2)	23.57 ± 1.19	0.93 ± 0.13	0.8860
	100 (step 1)	7.99 ± 1.08	8.33 ± 0.30	0.9960
	100 (step 2)	33.92 ± 1.88	1.87 ± 0.21	0.9267

3.7. Adsorption Kinetics

The study of adsorption kinetics offers valuable insights into the adsorption mechanism, which is essential for evaluating the effectiveness of the process. Initial studies reveal that the maximum level of adsorption is reached within 90 min, while the TC dosage is varied to assess the kinetic effects on the removal of TC. The kinetic models encompassed the pseudo-first-order, pseudo-second order, and intraparticle diffusion models. The pseudo-first-order kinetic model can be represented by the linear equation, which is expressed in the equation below [45],

$$ln(q_e - q_t) = lnq_e - k_1 t \quad (8)$$

The rate at which adsorption reaches equilibrium is represented by the equilibrium rate constant (k_1, min^{-1}). An adsorbent adsorption capacity is denoted by q_e (mg/g) at equilibrium and q_t (mg/g) at any given time t during the adsorption process. Kinetics plot of three distinct initial dosage of TC 20, 50, and 100 ppm are illustrated in Figure 5a. The kinetic parameters that were obtained are displayed in Table 5. The R^2 was found to be 0.9208, 0.9335, and 0.8015 for the concentrations of 20, 50, and 100 ppm, respectively. The experimental data displayed a lack of consistency with the pseudo-first-order model, indicating that the adsorption mechanism of TC on GGBS-Ox is not sufficiently explained by the pseudo-first-order model.

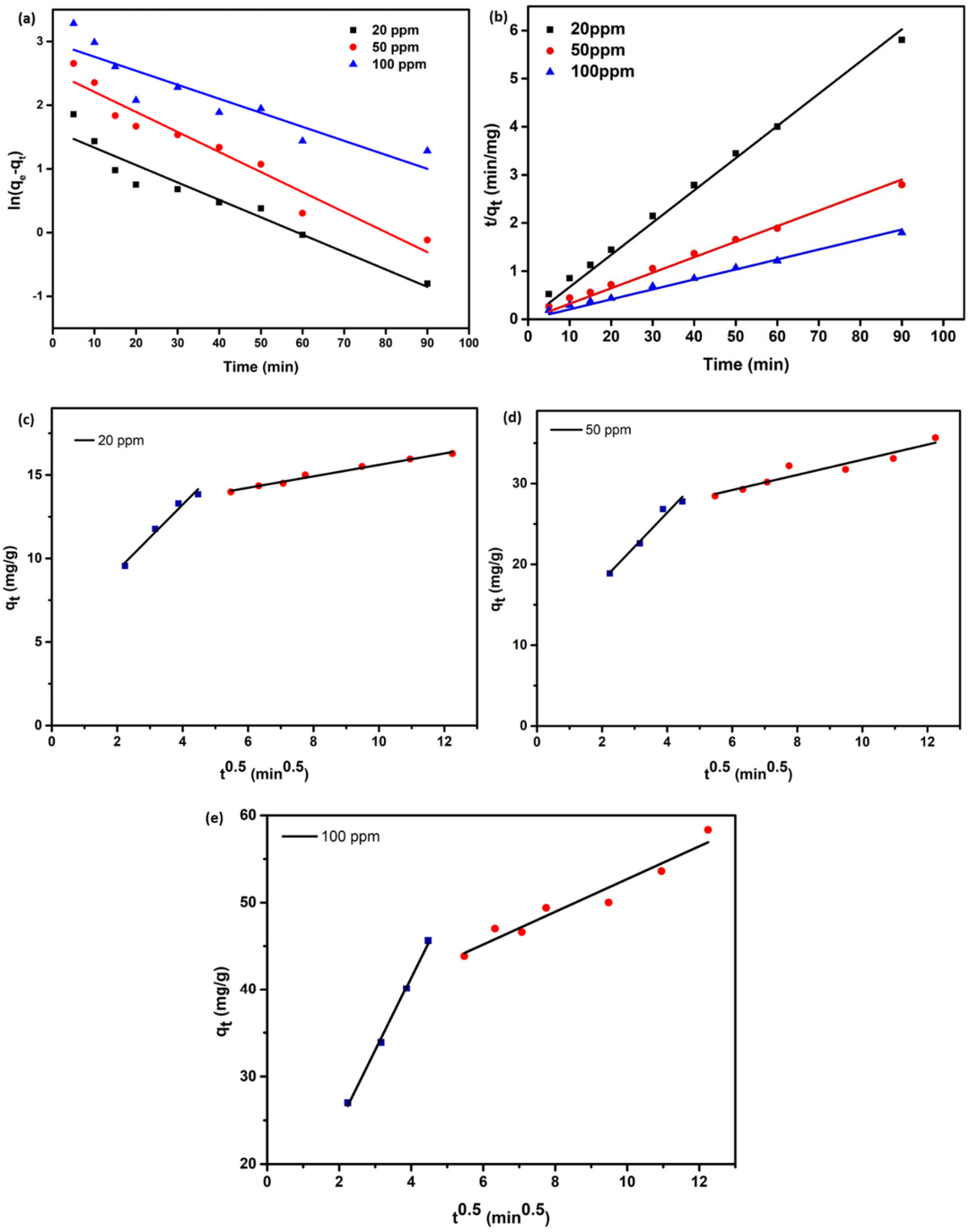

Figure 5. Kinetics of adsorption of TC (**a**) First-order kinetics, (**b**) Second-order kinetics and Intra-particle diffusion, (**c**) 20 ppm of TC, (**d**) 50 ppm of TC. (**e**) 100 ppm of TC.

The second-order kinetic model was applied for the obtained data using the following equation [11],

$$\frac{t}{q_t} = \frac{1}{k_2 q_e^2} + \frac{t}{q_e} \quad (9)$$

Figure 5b illustrates a linear plot to evaluate the adsorption kinetics parameters of the pseudo second-order model. The variables q_e and q_t (mg/g) respectively signify the adsorption capacity at equilibrium and time (t). Additionally, the equilibrium rate constant is represented by k_2 (g/mg/min). The results are presented in Table 5, displaying the R^2 for TC dosage of 20, 50, and 100 ppm as 0.9973, 0.9959, and 0.9955, respectively. Kinetic data about the adsorption of TC indicates that the pseudo second order is highly suitable for describing the process. Furthermore, the adsorption efficiency of TC is significantly impacted by the number of active sites present on the GGBS-Ox adsorbent [24].

Further, to validate the kinetics of adsorption, a range of dosages of adsorbent from 10 to 100 mg, in combination with TC dosage of 40 ppm, were tested for both first and second-order kinetics. Results of the tests showed that the second-order fits were accurate, as Figure S6 and Table S1 illustrate. Many other studies [11,46,47] have shown that second order models correlate the data for the adsorption of pollutants. Thus, it appears that second order models are better in fitting the experimental than first order models.

Pollutant uptake involves multiple steps, such as mass transfer of pollutant on to the adsorbent surface, intraparticle diffusion, and adsorption of pollutant on to the adsorbent sites [48]. To assess whether intraparticle diffusion serves as the limiting step in the adsorption of TC on the GGBS-Ox adsorbent, the intraparticle diffusion model was employed. The Weber and Morris intraparticle diffusion kinetic equation is as follows [49]:

$$q_t = k_i t^{1/2} + C_i \quad (10)$$

where K_i (mg/g (min)$^{1/2}$) represents the intraparticle diffusion rate constant, which is associated with the related constant C_i, indicating the boundary layer thickness. Both have a large effect on molecular diffusion. In Figure 5c–e, the intraparticle diffusion kinetic model is employed to analyze the adsorption process of tetracycline (TC) on the GGBS-Ox adsorbent across varying initial concentrations of TC. The graph of q_t versus $t^{1/2}$ displays two steps with various slopes, and the constants (K_i and C_i) for all steps are listed in Table 5. The experimental findings demonstrated that the two steps did not intersect at the origin, indicating that the main limitation of the adsorption process was not solely attributed to intraparticle diffusion. Instead, it was observed that both liquid-film and intraparticle diffusions play significant roles in the adsorption process. The initial linear section of the plot demonstrates how TC molecules diffuse from the main solution to the GGBS-Ox outer layer. The subsequent phase is referred to as intra-particle diffusion, wherein the TC molecules move through the absorbent's pores to get to the inner surface. The latter half relates to the achievement of equilibrium. The higher R^2 values signify that intra-particle diffusion was significantly involved in the adsorption process. Similar results were observed in the other investigations that have studied the adsorption of aquatic pollutants [48,50].

3.8. Adsorption Isotherms

Adsorption isotherms were utilized to establish a correlation between the equilibrium concentration of the TC solution at a particular temperature. These isotherms were fitted to models such as Langmuir, Freundlich, and DR isotherms. The initial concentration of TC was systematically altered within the range of 20 ppm to 100 ppm while keeping the adsorbent dosage and time constant. The monolayer adsorption phenomenon can be explained by employing the Langmuir isotherm, which is mathematically expressed by the subsequent equation [11]:

$$\frac{C_e}{q_e} = \frac{1}{q_m k_L} + \frac{1}{q_m} C_e \quad (11)$$

The variable q_e denotes the quantity of TC adsorbed on GGBS-Ox (mg/g). The C_e represents the equilibrium concentration (ppm), q_m represents the maximum adsorption capacity (mg/g), and k_L indicates the Langmuir equilibrium constant. The adsorption behavior of TC is visually depicted through Figure 6a, which presents the Langmuir isotherm plot. The parameters associated with the Langmuir equation are presented in Table 6.

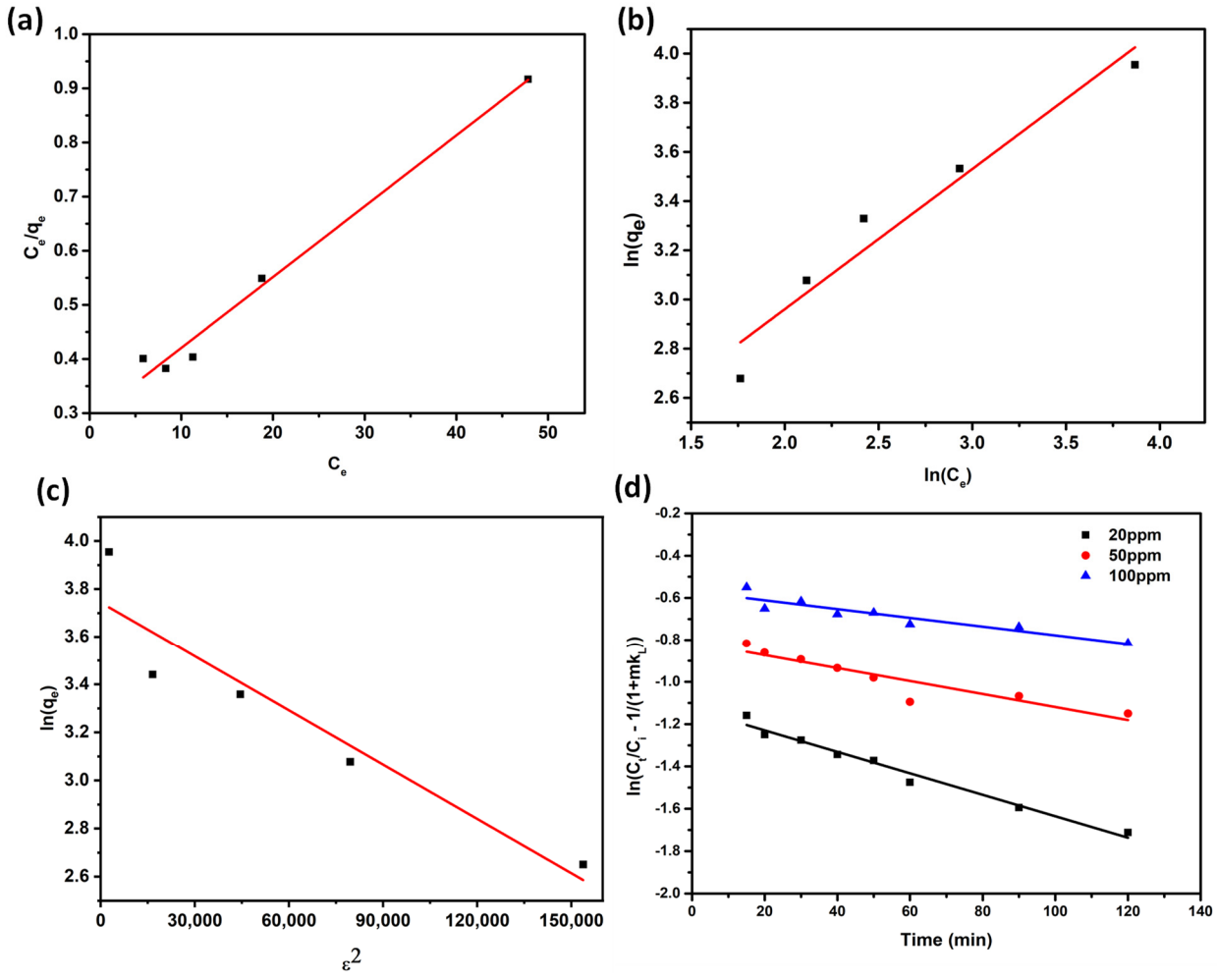

Figure 6. (**a**) Langmuir isotherm (**b**) Freundlich isotherm (**c**) DR isotherm and (**d**) McKay model.

Table 6. The parameters and regression coefficients for Langmuir, Freundlich, DR isotherm and McKay external diffusion model.

Isotherm Model	Parameters		Regression Coefficient
Langmuir	q_m: 76.3942	k_L: 0.0452	0.9820
Freundlich	n: 1.76	k_F: 6.18	0.9312
DR	B: 7.53×10^{-6}	E: 257 kJ/mol	0.8601
McKay	Concentration	Diffusion coefficient, cm^2/s (β)	
	20	3.812×10^{-9}	0.97
	50	2.310×10^{-9}	0.84
	100	1.564×10^{-9}	0.84

The Freundlich isotherm is a mathematical model which relies on the adsorption of a substance on a heterogeneous surface. This equation is used to calculate the adsorption, which occurs in multiple layers and is expressed as:

$$ln(q_e) = ln(k_F) + \frac{1}{n} ln(C_e) \quad (12)$$

In the above equation, the Freundlich adsorption constant is denoted as k_F, and the heterogeneity factor is represented by n. The equilibrium data points are subjected to linear fitting using the Freundlich models, as depicted in Figure 6b. For both the Langmuir and Freundlich models, Table 6 lists the experimental constants. The Langmuir model offers a better representation of the isotherm data, with a maximum adsorption capacity of 76.39 mg/g and a high determination coefficient (R^2) value (Figure 6). This confirms that the adsorption of TC onto GGBS-Ox involves a monolayer adsorption process. Many other studies [11,48] have shown that Langmuir isotherms correlate the data for the adsorption of various pollutants.

The experimental data were subjected to additional analysis using the Dubinin–Radushkevich isotherm (DR isotherm) technique [51]. The mathematical representation of the DR isotherm equation, in its linear form, is as follows:

$$ln(q_e) = ln(q_m) + \beta\varepsilon^2 \quad (13)$$

$$\varepsilon = RTln\left(1 + \frac{1}{C_e}\right) \quad (14)$$

where, q_m represents the adsorption capacity expressed in mg/g, β referred to as the DR isotherm constant, R indicates the universal gas constant and ε is the Polanyi potential. Figure 6c depicts the linear plots representing the DR isotherm. B also denotes the porosity factor, which is less than one (7.35×10^{-6} mol/kJ), indicating that the GGBS-Ox surface was micro-porous [45,52]. DR isotherm constant has a correlation to the mean free energy of adsorption, which is represented by $E = 1/(2\beta)^{0.5}$. Table 6 presents the free energy of adsorption. The computed correlation value ($R^2 = 0.89$) does not effectively align with the model. However, the energy determined (258 kJ/mol) is consistent with chemisorption behavior [45,51,53].

The study utilized the McKay model to investigate the impact of external diffusion on the adsorption mechanism. The mathematical formulation of this model is represented as follows:

$$ln\left(\frac{c_t}{c_i} - \frac{1}{1 + mk_l}\right) = ln\left(\frac{mk_l}{1 + mk_l}\right) - \left(\frac{1 + mk_l}{mk_l}\right)\beta_t S_s t \quad (15)$$

The concentrations of TC at different times (t) and initial time ($t = 0$) are denoted by C_t and C_i, respectively. The variable m represents the adsorbent (g/L), while S_s indicates the SSA of the adsorbent per unit volume of the TC solution (cm^{-1}). β_t corresponds to the external diffusion coefficient (cm^2/s), and k_l is the Langmuir constant derived from the Langmuir isotherm (L g^{-1}). The linear correlation of $\left(\frac{c_t}{c_i} - \frac{1}{1+mk_l}\right)$ with time, as Figure 6d illustrates, provides supporting evidence for the applicability of the McKay model in examining external diffusion [51]. Furthermore, it was validated that external diffusion significantly influences TC adsorption, surpassing intraparticle diffusion. Nevertheless, the mass transfer from the bulk solution to the surface transpires rapidly, indicating that it is not the limiting step in the overall process. The diffusion coefficients, which signify the amount of pollutant adsorbed onto the surface as a function of time, are presented in Table 6.

3.9. Reusability of Adsorbent

In order to use adsorption technology in practical applications, adsorbent recycling tests are a prerequisite. A crucial element in the economic viability of these technologies

is the adsorbent reusability [32]. Adsorbents can be recovered and reused multiple times without losing their effectiveness and efficiency. The used GGBS-Ox was washed with 20 mL of 20% ethanol solvent at the end of every cycle [54] and dried in an oven at 60 °C for 24 h. Results show that the GGBS-Ox could be reused with no considerable decrease in its adsorption capacity since the removal effectiveness remained high (65%) even after the five consecutive adsorption-desorption sequences, as Figure 7a shows. The GGBS-Ox, after the adsorption of TC, is regenerated in an environmentally friendly and sustainable manner, promoting the circular process for multiple usage by reusing the resource.

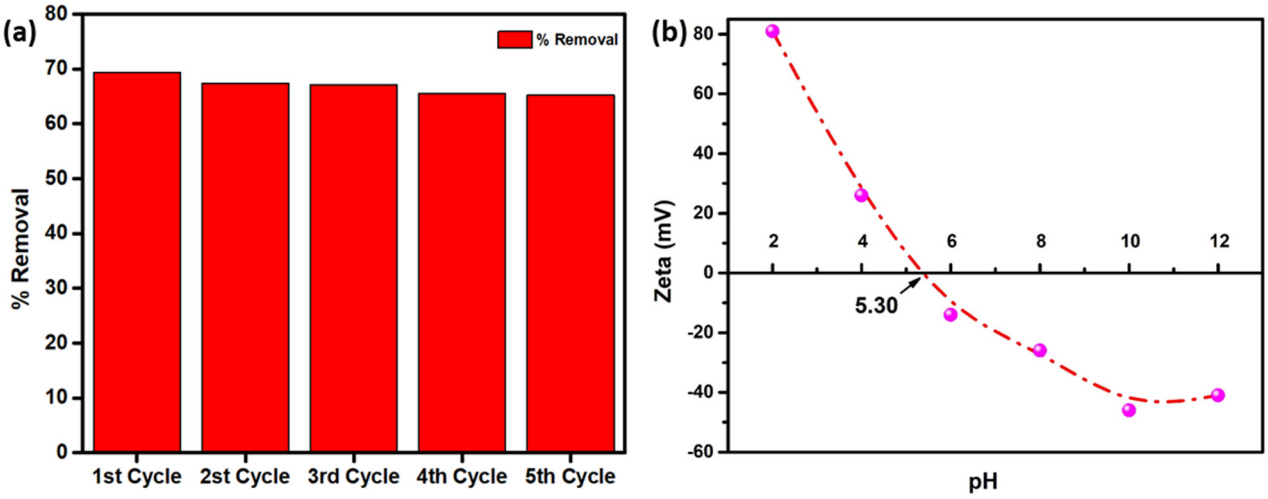

Figure 7. (**a**) Regeneration of GGBS-Ox (**b**) Zeta potential as a function of pH and PZC for GGBS−Ox.

3.10. Point of Zero Charge

The ionization state of adsorbates and the surface charge have been observed to exhibit pH dependence. The pH at which the adsorbent surface will have neutral charge is known as the point of zero charge (PZC). The determination of the pH_{pzc} (pH at the point of zero charge) value is of utmost importance in order to ascertain the pH intervals in which the surface charge of the adsorbent demonstrates either positive or negative charge [55]. The surfaces of GGBS-Ox will exhibit a negative charge when the pH of the solution is above the PZC. Conversely, these surfaces will display a positive charge when the pH of the solution is below the PZC [55]. Using the influence of surface charges on the GGBS-Ox, PZC was determined to be 5.30 as shown in Figure 7b. It suggests that the adsorbent has a slightly negative charge at pH levels above 5.30, which could facilitate the adsorption of tetracycline.

3.11. Adsorption Thermodynamics

To evaluate the thermodynamic parameters of tetracycline adsorption on GGBS-Ox, experiments were conducted at three distinct temperatures. The outcomes of these experiments are useful for comprehending the mechanism of TC adsorption on GGBS-Ox. The thermodynamic parameters, such as Gibbs free energy (ΔG°), enthalpy (ΔH°), and entropy (ΔS°), were graphically calculated using Gibbs free energy and Van't Hoff equations.

$$\Delta G^{o} = -RTlnK_{d} \quad (16)$$

$$\Delta G^{o} = \Delta H - T\Delta S^{o} \quad (17)$$

$$lnk = \frac{\Delta S^{o}}{R} - \frac{\Delta H^{o}}{RT} \quad (18)$$

where K_d is used to denote the equilibrium constant. The gas constant, denoted by the symbol R, possesses a numerical value of 8.314 J/mol.K, and T is used to signify the absolute temperature (K). Table 7 presents the thermal parameters obtained through the

plot, as illustrated in Figure S8. The observation of a negative ΔG° value suggests that the process of adsorption is inherently spontaneous [11]. The increasing temperature trend was beneficial to the absorption process. The enthalpy change (ΔH°) determined was greater than zero, affirming the endothermic nature of adsorption. Lower ΔH° (5.1169 kJ mol^{-1}) values indicate that TC and GGBS-Ox are undergoing physisorption since the value of ΔH° varies between 5 and 20 kJ/mol [16]. The positive value of entropy during the process (ΔS° = 0.1119 kJ/mol K) indicated a disordering and random tendency, as well as a strong affinity between TC and GGBS-Ox during the course of adsorption [56].

Table 7. Thermodynamic conditions for GGBS-Ox adsorption at different temperatures.

Temperature (K)	1/T	lnK_d	ΔG° (kJ/mol)	ΔH° (kJ/mol)	ΔS° (kJ/mol K)	R^2
298	0.003356	11.3942	−28.2299			
308	0.003247	11.4602	−29.3462	5.1169	0.1119	0.9998
318	0.003145	11.5241	−30.4680			

3.12. Mechanism of Adsorption

The results from McKay's and interparticle diffusion models demonstrated that the process of TC adsorption is a multiple-step procedure. Thermodynamic analysis showed that the adsorption exhibits characteristics of spontaneity and endothermicity. In addition, FTIR measurements were conducted both before and after adsorption of TC to examine the adsorption mechanism. This experimental procedure is illustrated in Figure 8a. The FTIR spectra of TC adsorbed on GGBS-Ox shows a new characteristic bond at 1460 cm^{-1}. This bond is ascribed to the vibration of the aromatic ring of TC, indicating the presence of TC on the surface of GGBS-Ox [57,58]. Furthermore, the characteristic bonds of Si-O-Si, Si-O-Al, and Si-OH are shifted to new positions due to the adsorption of TC. Additionally, the migration of different peaks of hydroxyl group (–OH), such as Si-O-Al and Si-OH, are seen to be weakened after the adsorption of TC, indicating that the hydroxyl group is also involved in the adsorption reaction as it will form electrostatic interactions with the TC. Moreover, the oxygen-containing functional groups, such as $CO_3{}^{-2s}$, Si-O-Si, Si-O-Al, and Si-OH bonds, facilitate interactions with the amino group, carboxyl group, benzene ring, and acid-base groups present in the TC molecule. These interactions occur through the formation of hydrogen bonds during the reaction, which consequently leads to a discernible shift in the peak positions recorded in the spectra [59]. To further investigate the adsorption of TC, XPS analyses of GGBS-Ox were conducted before and after adsorption. The full scan spectrum of samples is shown in Figure 8b. After adsorption of TC, the majority of peaks shifted to lower binding energies, indicating electrostatic interaction [60]. The decreased peak area of O 1s indicates that surface functional groups participate in the adsorption of TC [61].

The PZC of GGBS-Ox observed at 5.3 reveals that the adsorbent will be negatively charged at a pH above 5.3. TC is an amphoteric organic substance because it contains both weak bases and weakly acidic functional groups. These functional groups allow TC to act as both a positive and negative charge, depending on the pH of the solution [62]. Based on the pH of the solution, tetracycline (TC) exhibits distinct ionization states characterized by three different pKa values, namely 3.3, 7.7, and 9.7. At pH levels below 3.3, TC is predominantly observed in the form of TCH_3^+. Between pH 3.3 and 7.7, it exists as TCH_2^0, while in the pH range of 7.7 to 9.7, it takes the form of TCH^-. Finally, at pH above 9.7, TC is present as TC^{-2} [63]. Tetracycline adsorption on GGBS-Ox is significantly influenced by the pH of the solution. The high concentration of H^+ ions in the solution creates hydrogen bonds with the TC molecule at an acidic pH, which causes the TC molecule and the functional groups on the surface of the adsorbent to repel one another electrostatically, leading to lower adsorption [63]. In the neutral pH range, the adsorption of TC onto GGBS-Ox is primarily facilitated by hydrogen bonding interactions between TCH_2^0 and the OH groups on the surface of GGBS-Ox. Notably, the highest efficiency of TC removal

is observed at pH 7, emphasizing the significance of neutral pH conditions for optimal TC adsorption onto GGBS-Ox. The extremely hydrophobic zutrion species (TCH_2^0) of the tetracycline molecule reacts with adsorbent functional groups and increases adsorption capacity in neutral circumstances [54]. At higher pH, levels in the TC will be predominately natively charged (TCH^- and TC^{-2}), and GGBS-Ox is also negatively charged, which leads to electrostatic repulsion force between the similar charges (negative–negative), decreasing removal efficiency. In summary (Figure 8c), the adsorption of TC onto GGBS-Ox was predominated by pore-filling, H-bonding interactions, and electrostatic interactions.

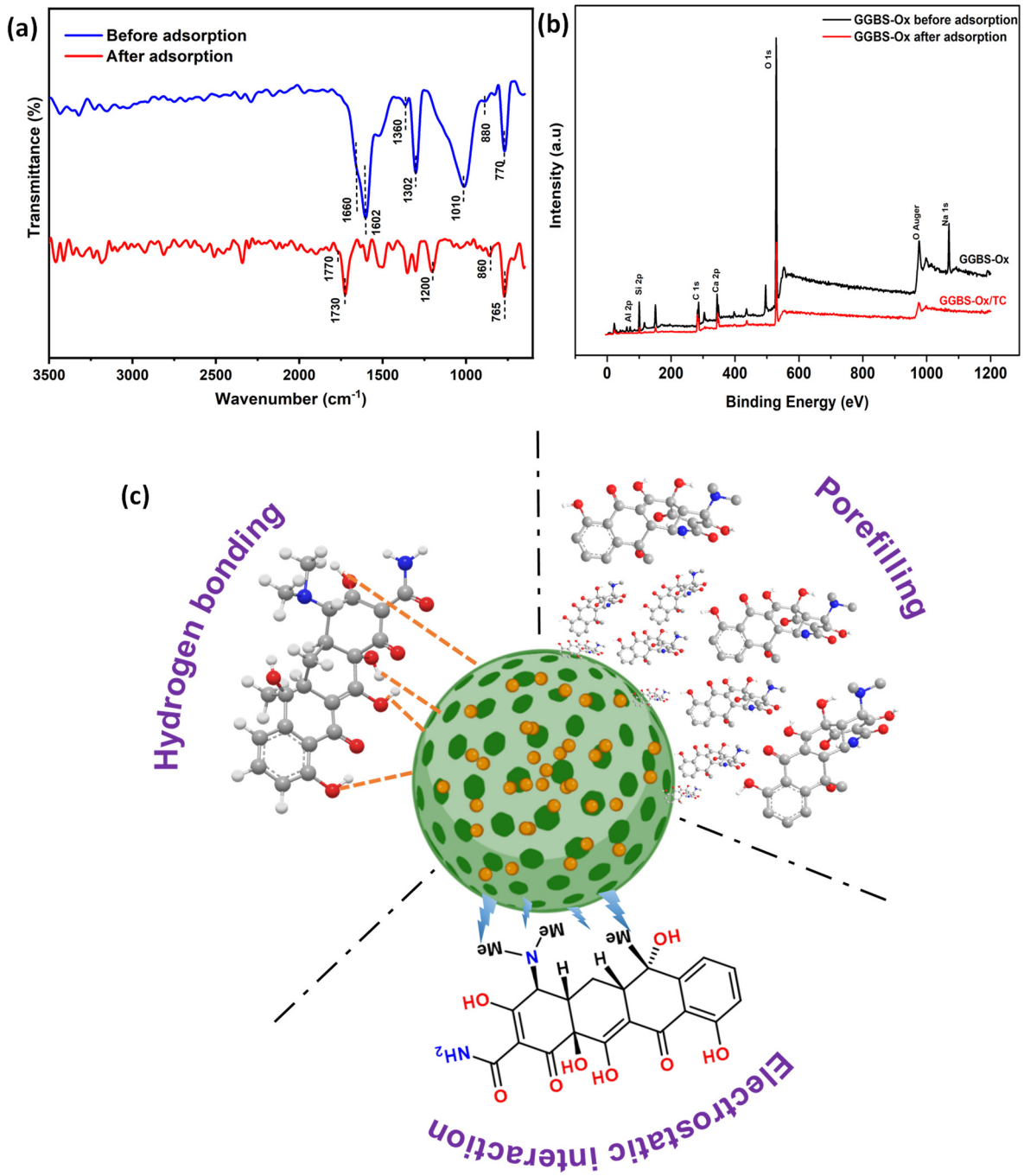

Figure 8. (**a**) FTIR for GGBS−Ox before and after adsorption of TC; (**b**) XPS full scan spectra for GGBS−Ox before and after adsorption of TC; (**c**) Plausible TC removal mechanisms using GGBS−Ox.

3.13. Comparison of the GGBS-Ox and Other Adsorbents Adsorption Parameters

The results of GGBS-Ox's adsorption of TC are compared with the adsorption parameters of other adsorbents, as Table 8 shows. Table 8a illustrates the adsorption of TC by various adsorbents, and Table 8b demonstrates the adsorption of a wide variety of contaminants by various categories of iron industrial waste-based adsorbent. This table shows that using non-conventional waste-based adsorbents makes it difficult to completely remove TC from water. The composite of industrial waste with biochar shows higher removal due to its higher surface area. However, when this same industrial waste-based adsorbent is used to remove dyes and metal ions, 100 percent adsorption was observed. GGBS-Ox can be a better adsorbent than some graphene oxide composites (GO/CA) and is much cheaper. The comparison suggests that GGBS-Ox is an effective adsorbent with a high removal rate that can be applied for the adsorption of numerous water pollutants and is reusable. GGBS-based adsorbent will also help make the adsorption process economical compared to other adsorbents due to its abundance.

Table 8. Adsorption capacities for (a) TC adsorption using various adsorbents and (b) various water pollutants using GGBS.

Adsorbent	Pollutant	Dosage of Adsorbent (g/L)/Pollutant (ppm)	Adsorption Capacity	% Removal	Reference
(a) Adsorption of TC using various adsorbents					
Biochar from microalgae	TC	1200/20	13.6	58	[43]
Pharmaceutical sludge-derived biochar	TC	1/200	94.70 157.4	47 78	[64]
Rice husk ash	TC	2/20	3.41	34	[65]
Polymeric adsorbent derived from the rubber waste	TC	0.75/20	30	100	[47]
NaOH-modified steel dust	TC	1/30	14 20	-	[16]
Sludge biochar	TC	0.25/20	30	80	[50]
Graphene oxide/calcium alginate composite fibers	TC	0.6/50	-	63	[66]
(b) Adsorption of various water pollutants using GGBS					
Steel dust wastes	Eriochrome Black T dye	0.4/20	100	100	[67]
Calcium silicate hydrate (CSH)—Cu(II)	Methylene blue	0.25/20	-	90	[68]
Biochar-steel dust composite	Phosphate	0.166/100	175	-	[21]
Steel slag	Phosphorus	7.5/50	18	99	[69]
Slag-Oxalate	Co^{2+}	1/30	576	-	[33]
GGBS-Ox	TC	1/20	15.9	68	This study

4. Conclusions

The present investigation demonstrated the successful synthesis of GGBS-Ox and its subsequent application for the removal of TC from an aqueous solution. The prepared adsorbent underwent characterization through various techniques including FTIR, XRD, SEM, DLS, and XPS. The preliminary adsorption studies showed the higher removal of TC (68%) at an optimum adsorbent and pollutant dosage of 50 mg and 20 ppm, respectively. RSM incorporating BBD, ANN, and RF were successfully employed to evaluate the influence of three chosen independent variables, such as pH, stirring speed, and time, on the adsorption process. Statistical tools such as R^2, RMSE, and MEA were employed to evaluate the models. All models show that pH plays a key role in the adsorption process, and there is minimal effect from time and stirring speed. The RSM-based BBD was determined to be reliable (R^2 = 0.98) in predicting the percentage removal of TC compared to RF (R^2 = 0.98) and RSM (R^2 = 0.95). The kinetic and isotherm data suggested that the adsorption of

TC was predominantly controlled by the pseudo-second order adsorption mechanism (R^2 = 0.99) and Langmuir model (R^2 = 0.98), indicating faster and monolayer adsorption. Thermodynamic study indicates that the adsorption is endothermic and spontaneous in nature. The studies show that the GGBS-Ox can be applied for the adsorption of TC due to its efficiency, availability, reusability, and cost-effectiveness.

Supplementary Materials: The following supporting information can be downloaded at: https://www.mdpi.com/article/10.3390/su16010464/s1, Figure S1. (a) Artificial neural network architecture for modeling the adsorption of TC into GGBS-Ox (b) Random forest architecture for modeling the adsorption of TC into GGBS-Ox; Figure S2. N_2 adsorption and desorption isotherms of GGBS and GGBS-Ox; Figure S3. N_2 adsorption/desorption curves of different adsorbents (insert: pore size distrubtion). (Page S10); Figure S3. (a) Particle size distribution by dynamic light scattering (DLS) of GGBS (b) Particle size distribution by dynamic light scattering (DLS) of GGBS-Ox; Figure S4. (a) The effect of adsorbent dosage on percentage removal (b) the effect of pollutant concentration on the percentage removal; Figure S5. (a) Comparison of predicted and actual results for RSM (b) Comparison of predicted and actual results for ANN (c) Comparison of predicted and actual results for RF; Figure S6. Perturbation plot for TC removal efficiency; Figure S7. Kinetics of adsorption of TC (a) First-order kinetics (b) Second-order kinetics; Figure S8. Effect of the temperature on the adsorption capacity of TC by GGBS-Ox; Figure S9. Thermodynamic parameters of TC adsorption by GGBS-Ox; Table S1. Levels of parameters for BBD experiments; Table S2. Comparison of RSM, ANN, and RF; Table S3. Calculation of adsorption parameters and regression coefficients; Table S4. The parameters and regression coefficients for pseudo-first order and pseudo-second order; Table S5. The parameters and regression coefficients for Langmuir, Freundlich, DR isotherm and McKay external diffusion model; Table S6. Thermodynamic conditions for GGBS-Ox adsorption at different temperatures.

Author Contributions: Conceptualization, C.S., C.L. and H.S.R.; methodology, C.S., C.L., P.P.M. and H.S.R.; software, G.M. and H.S.R.; validation, C.L., P.P.M. and C.S.; formal analysis, I.H.; investigation, H.S.R.; resources, C.S.; data curation, C.S., C.L. and G.M.; writing—original draft preparation, H.S.R.; writing—review and editing, C.S., I.H. and G.M.; visualization, P.P.M. and I.H.; supervision, C.S. and C.L.; project administration, C.S.; funding acquisition, C.S. All authors have read and agreed to the published version of the manuscript.

Funding: This research received no external funding.

Institutional Review Board Statement: Not applicable.

Informed Consent Statement: Not applicable.

Data Availability Statement: Data can be made available upon request.

Acknowledgments: Harsha, S.R. would like to thank the Indian Institute of Technology Hyderabad and Deakin University for the research facilities and financial support. Harsha, S.R. would like to thank Sri Rama Murty K for the software support.

Conflicts of Interest: The authors declare no conflicts of interest.

Abbreviations

GGBS: Ground granulated blast furnace slag, GGBS-Ox: Ground granulated blast furnace slag oxalate, TC: Tetracycline, RSM: Response Surface Methodology, BBD: Box–Behnken design, ANN: Artificial neural network, RF: Random forest, FTIR: Fourier Transform Infrared, XRD: X-ray diffraction, SEM: Scanning Electron Microscope, XPS: X-ray photoelectron spectroscopy, DLS: Dynamic light scattering, R^2: Determination coefficients, DR: Dubinin–Radushkevich, RBF-NN: Radial Basis Function Neural Network, SSA: specific surface area, CCD: Central Composite Design, PZC: Point of Zero Charge, ANOVA: Analysis of variance, SD: standard deviation, RMSE: Root Mean Square Error, MAE: mean absolute error, EBT: Eriochrome black T.

References

1. Balakrishnan, A.; Chinthala, M.; Polagani, R.K.; Vo, D.V.N. Removal of Tetracycline from Wastewater Using G-C_3N_4 Based Photocatalysts: A Review. *Environ. Res.* **2023**, *216*, 114660. [CrossRef] [PubMed]
2. Koch, N.; Islam, N.F.; Sonowal, S.; Prasad, R.; Sarma, H. Environmental Antibiotics and Resistance Genes as Emerging Contaminants: Methods of Detection and Bioremediation. *Curr. Res. Microb. Sci.* **2021**, *2*, 100027. [CrossRef] [PubMed]
3. Patel, M.; Kumar, R.; Kishor, K.; Mlsna, T.; Pittman, C.U.; Mohan, D. Pharmaceuticals of Emerging Concern in Aquatic Systems: Chemistry, Occurrence, Effects, and Removal Methods. *Chem. Rev.* **2019**, *119*, 3510–3673. [CrossRef] [PubMed]
4. Phoon, B.L.; Ong, C.C.; Mohamed Saheed, M.S.; Show, P.L.; Chang, J.S.; Ling, T.C.; Lam, S.S.; Juan, J.C. Conventional and Emerging Technologies for Removal of Antibiotics from Wastewater. *J. Hazard. Mater.* **2020**, *400*, 122961. [CrossRef]
5. Rout, P.R.; Zhang, T.C.; Bhunia, P.; Surampalli, R.Y. Treatment Technologies for Emerging Contaminants in Wastewater Treatment Plants: A Review. *Sci. Total Environ.* **2021**, *753*, 141990. [CrossRef]
6. Dhangar, K.; Kumar, M. Tricks and Tracks in Removal of Emerging Contaminants from the Wastewater through Hybrid Treatment Systems: A Review. *Sci. Total Environ.* **2020**, *738*, 140320. [CrossRef]
7. Qin, J.; Wang, X.; Deng, M.; Li, H.; Lin, C. Red Mud-Biochar Composites (Co-Pyrolyzed Red Mud-Plant Materials): Characteristics and Improved Efficacy on the Treatment of Acidic Mine Water and Trace Element-Contaminated Soils. *Sci. Total Environ.* **2022**, *844*, 157062. [CrossRef]
8. Shahid, M.K.; Kashif, A.; Fuwad, A.; Choi, Y. Current Advances in Treatment Technologies for Removal of Emerging Contaminants from Water—A Critical Review. *Coord. Chem. Rev.* **2021**, *442*, 213993. [CrossRef]
9. Siyal, A.A.; Shamsuddin, M.R.; Khan, M.I.; Rabat, N.E.; Zulfiqar, M.; Man, Z.; Siame, J.; Azizli, K.A. A Review on Geopolymers as Emerging Materials for the Adsorption of Heavy Metals and Dyes. *J. Environ. Manage.* **2018**, *224*, 327–339. [CrossRef]
10. Senthil Kumar, P.; Janet Joshiba, G.; Femina, C.C.; Varshini, P.; Priyadharshini, S.; Arun Karthick, M.S.; Jothirani, R. A Critical Review on Recent Developments in the Low-Cost Adsorption of Dyes from Wastewater. *Desalin. Water Treat.* **2019**, *172*, 395–416. [CrossRef]
11. Phyu Mon, P.; Phyu Cho, P.; Chanadana, L.; Ashok Kumar, K.V.; Dobhal, S.; Shashidhar, T.; Madras, G.; Subrahmanyam, C. Bio-Waste Assisted Phase Transformation of Fe_3O_4/Carbon to NZVI/Graphene Composites and Its Application in Reductive Elimination of Cr(VI) Removal from Aquifer. *Sep. Purif. Technol.* **2023**, *306*, 122632. [CrossRef]
12. Manoj Kumar Reddy, P.; Mahammadunnisa, S.; Ramaraju, B.; Sreedhar, B.; Subrahmanyam, C. Low-Cost Adsorbents from Bio-Waste for the Removal of Dyes from Aqueous Solution. *Environ. Sci. Pollut. Res.* **2013**, *20*, 4111–4124. [CrossRef] [PubMed]
13. Yao, Y.; Wang, Y.; Wei, Q.; Cui, S.; Hao, L. Effect of the Formation of Amorphous Networks on the Structure and Hydration Characteristics of Granulated Blast Furnace Slag. *Materials* **2020**, *13*, 1462. [CrossRef] [PubMed]
14. Han, H.; Rafiq, M.K.; Zhou, T.; Xu, R.; Mašek, O.; Li, X. A Critical Review of Clay-Based Composites with Enhanced Adsorption Performance for Metal and Organic Pollutants. *J. Hazard. Mater.* **2019**, *369*, 780–796. [CrossRef] [PubMed]
15. Özbay, E.; Erdemir, M.; Durmuş, H.I. Utilization and Efficiency of Ground Granulated Blast Furnace Slag on Concrete Properties—A Review. *Constr. Build. Mater.* **2016**, *105*, 423–434. [CrossRef]
16. Saood Manzar, M.; Ahmad, T.; Ullah, N.; Velayudhaperumal Chellam, P.; John, J.; Zubair, M.; Brandão, R.J.; Meili, L.; Alagha, O.; Çevik, E. Comparative Adsorption of Eriochrome Black T and Tetracycline by NaOH-Modified Steel Dust: Kinetic and Process Modeling. *Sep. Purif. Technol.* **2022**, *287*, 120559. [CrossRef]
17. Ibrahim, M.M.; El, H.S.; Mahmoud, S.; El, O.A.; El, M.; Manaa, S.A.; Youssef, M.A.M.; Kouraim, M.N.; Eldesouky, E.M.; Dhmees, A.S. A Facile and Cost-Effective Adsorbent Derived from Industrial Iron-Making Slag for Uranium Removal. *J. Radioanal. Nucl. Chem.* **2021**, *329*, 1291–1300. [CrossRef]
18. Gupta, V.K.; Ali, I.; Saini, V.K. Adsorption of 2, 4-D and Carbofuran Pesticides Using Fertilizer and Steel Industry Wastes. *J. Colloid Interface Sci.* **2006**, *299*, 556–563. [CrossRef]
19. Bhuyan, M.A.H.; Gebre, R.K.; Finnilä, M.A.J.; Illikainen, M.; Luukkonen, T. Preparation of Filter by Alkali Activation of Blast Furnace Slag and Its Application for Dye Removal. *J. Environ. Chem. Eng.* **2022**, *10*, 107051. [CrossRef]
20. Manthiram Karthik, R.; Philip, L. Sorption of Pharmaceutical Compounds and Nutrients by Various Porous Low Cost Adsorbents. *J. Environ. Chem. Eng.* **2021**, *9*, 104916. [CrossRef]
21. Zubair, M.; Saood, M.; Awwal, M.; Pinto, D.; Meili, L.; Al, W.; Essa, B.; Al-adam, H.; Alghamdi, J.M.; Dalhat, N.; et al. Production of Magnetic Biochar-Steel Dust Composites for Enhanced Phosphate Adsorption. *J. Water Process Eng.* **2022**, *47*, 102793. [CrossRef]
22. Gameiro, T.; Costa, C.; Labrincha, J.; Novais, R.M. Reusing Spent Fluid Catalytic Cracking Catalyst as an Adsorbent in Wastewater Treatment Applications. *Mater. Today Sustain.* **2023**, *24*, 100555. [CrossRef]
23. Osman, A.I.; Elgarahy, A.M.; Mehta, N.; Al-muhtaseb, A.H.; Al-fatesh, A.S.; Rooney, D.W. Facile Synthesis and Life Cycle Assessment of Highly Active Magnetic Sorbent Composite Derived from Mixed Plastic and Biomass Waste for Water Remediation. *ACS Sustain. Chem. Eng.* **2022**, *10*, 12433–12447. [CrossRef] [PubMed]
24. Allouss, D.; Essamlali, Y.; Amadine, O.; Chakir, A.; Zahouily, M. Response Surface Methodology for Optimization of Methylene Blue Adsorption onto Carboxymethyl. *RSC Adv.* **2019**, *9*, 37858–37869. [CrossRef] [PubMed]
25. Kalavathy, H.; Regupathi, I.; Ganesa, M.; Rose, L. Modelling, Analysis and Optimization of Adsorption Parameters for H_3PO_4 Activated Rubber Wood Sawdust Using Response Surface Methodology (RSM). *Colloids Surf. B Biointerfaces* **2009**, *70*, 35–45. [CrossRef] [PubMed]

26. Aghav, R.M.; Kumar, S.; Mukherjee, S.N. Artificial Neural Network Modeling in Competitive Adsorption of Phenol and Resorcinol from Water Environment Using Some Carbonaceous Adsorbents. *J. Hazard. Mater.* **2011**, *188*, 67–77. [CrossRef] [PubMed]
27. Ahmad, M.W.; Mourshed, M.; Rezgui, Y. Trees vs. Neurons: Comparison between Random Forest and ANN for High-Resolution Prediction of Building Energy Consumption. *Energy Build.* **2017**, *147*, 77–89. [CrossRef]
28. Elijah, C.; Nwabanne, J.T.; Ohale, P.E.; Asadu, C.O. Comparative Analysis of RSM, ANN and ANFIS and the Mechanistic Modeling in Eriochrome Black-T Dye Adsorption Using Modified Clay. *S. Afr. J. Chem. Eng.* **2021**, *36*, 24–42. [CrossRef]
29. Geyikc, F. Modelling of Lead Adsorption from Industrial Sludge Leachate on Red Mud by Using RSM and ANN. *Chem. Eng. J.* **2012**, *183*, 53–59. [CrossRef]
30. Ahmadi Azqhandi, M.H.; Ghaedi, M.; Yousefi, F.; Jamshidi, M. Application of Random Forest, Radial Basis Function Neural Networks and Central Composite Design for Modeling and/or Optimization of the Ultrasonic Assisted Adsorption of Brilliant Green on ZnS-NP-AC. *J. Colloid Interface Sci.* **2017**, *505*, 278–292. [CrossRef]
31. Chen, X.; Zhang, X.; Li, F.; Yang, X.; Du, M.; Fan, J. Material with Abundant Reaction Sites and Its Efficient Pb(II) Removal from Diverse Water Bodies. *New J. Chem.* **2022**, *46*, 8566–8574. [CrossRef]
32. Le, Q.T.N.; Vivas, E.L.; Cho, K. Calcium Oxalate/Calcium Silicate Hydrate (Ca-Ox/C-S-H) from Blast Furnace Slag for the Highly Efficient Removal of Pb^{2+} and Cd^{2+} from Water. *J. Environ. Chem. Eng.* **2021**, *9*, 106287. [CrossRef]
33. Thi, Q.; Le, N.; Vivas, E.L.; Cho, K. Oxalated Blast-Furnace Slag for the Removal of Cobalt (II) Ions from Aqueous Solutions. *J. Ind. Eng. Chem.* **2021**, *95*, 57–65. [CrossRef]
34. Azari, A.; Hassan, M.; Hazrati, M.; Eş, I. Rapid and Efficient Ultrasonic Assisted Adsorption of Diethyl Phthalate onto Fe II Fe^{2III} O_4 @GO: ANN-GA and RSM-DF Modeling, Isotherm, Kinetic and Mechanism Study. *Microchem. J.* **2019**, *150*, 104144. [CrossRef]
35. De Miranda Ramos Soares, A.P.; De Oliveira Carvalho, F.; De Farias Silva, C.E.; Da Silva Gonçalves, A.H.; De Souza Abud, A.K. Random Forest as a Promising Application to Predict Basic-Dye Biosorption Process Using Orange Waste. *J. Environ. Chem. Eng.* **2020**, *8*, 103952. [CrossRef]
36. Alam, G.; Ihsanullah, I.; Naushad, M.; Sillanpää, M. Applications of Artificial Intelligence in Water Treatment for Optimization and Automation of Adsorption Processes: Recent Advances and Prospects. *Chem. Eng. J.* **2022**, *427*, 130011. [CrossRef]
37. Lei, Z.; Wei, K.; Yang, J.; Zhang, L.; Lu, X.; Fang, B. Ultrasonication-Assisted Preparation of a Mn-Based Blast Furnace Slag Catalyst: Effects on the Low-Temperature Selective Catalytic Reduction Denitration Process. *ACS Omega* **2021**, *6*, 23059–23066. [CrossRef]
38. Zhang, Y.J.; Zhao, Y.L.; Li, H.H.; Xu, D.L. Structure Characterization of Hydration Products Generated by Alkaline Activation of Granulated Blast Furnace Slag. *J. Mater. Sci.* **2008**, *43*, 7141–7147. [CrossRef]
39. Yasipourtehrani, S.; Strezov, V.; Evans, T. Investigation of Phosphate Removal Capability of Blast Furnace Slag in Wastewater Treatment. *Sci. Rep.* **2019**, *9*, 7498. [CrossRef]
40. Elias, A. Amine Responsive Poly(Lactic Acid) (PLA) and Succinic Anhydride (SAh) Graft-Polymer: Synthesis and Characterization. *Polymers* **2019**, *11*, 1466.
41. Yang, S.; Cheng, Q.; Hu, L.; Gu, Y.; Wang, Y.; Liu, Z. Study on the Adsorption Properties of Oxalic Acid-Modified Cordierite Honeycomb Ceramics for Neutral Red Dyes. *ACS Omega* **2023**, *8*, 11457–11466. [CrossRef] [PubMed]
42. Althumayri, K.; Guesmi, A.; El-Fattah, W.A.; Houas, A.; Hamadi, N.B.; Shahat, A. Enhanced Adsorption and Evaluation of Tetracycline Removal in an Aquatic System by Modified Silica Nanotubes. *ACS Omega* **2023**, *8*, 6762–6777. [CrossRef] [PubMed]
43. Chabi, N.; Baghdadi, M.; Sani, A.H.; Golzary, A.; Hosseinzadeh, M. Removal of Tetracycline with Aluminum Boride Carbide and Boehmite Particles Decorated Biochar Derived from Algae. *Bioresour. Technol.* **2020**, *316*, 123950. [CrossRef] [PubMed]
44. Maldonado-rubio, M.I.; Guerra-sa, R.; Saldan, A.; Peralta-herna, J.M. Optimization of the Operating Parameters Using RSM for the Fenton Oxidation Process and Adsorption on Vegetal Carbon of MO Solutions. *J. Ind. Eng. Chem.* **2014**, *20*, 848–857. [CrossRef]
45. Singh, S.A.; Vemparala, B.; Madras, G. Adsorption Kinetics of Dyes and Their Mixtures with Co_3O_4-ZrO_2 Composites. *J. Environ. Chem. Eng.* **2015**, *3*, 2684–2696. [CrossRef]
46. Mahmood, T.; Din, S.U.; Naeem, A.; Tasleem, S.; Alum, A.; Mustafa, S. Kinetics, Equilibrium and Thermodynamics Studies of Arsenate Adsorption from Aqueous Solutions onto Iron Hydroxide. *J. Ind. Eng. Chem.* **2014**, *20*, 3234–3242. [CrossRef]
47. Aliyu, M.; Abdullah, A.H.; Tahir, M.I. bin M. Adsorption Tetracycline from Aqueous Solution Using a Novel Polymeric Adsorbent Derived from the Rubber Waste. *J. Taiwan Inst. Chem. Eng.* **2022**, *136*, 104333. [CrossRef]
48. Tanzifi, M.; Hosseini, S.H.; Kiadehi, A.D.; Olazar, M.; Karimipour, K.; Rezaiemehr, R.; Ali, I. Artificial Neural Network Optimization for Methyl Orange Adsorption onto Polyaniline Nano-Adsorbent: Kinetic, Isotherm and Thermodynamic Studies. *J. Mol. Liq.* **2017**, *244*, 189–200. [CrossRef]
49. Khademi, Z.; Ramavandi, B.; Taghi, M. The Behaviors and Characteristics of a Mesoporous Activated Carbon Prepared from Tamarix Hispida for Zn (II) Adsorption from Wastewater. *Biochem. Pharmacol.* **2015**, *3*, 2057–2067. [CrossRef]
50. Ma, Y.; Lu, T.; Tang, J.; Li, P.; Mašek, O.; Yang, L.; Wu, L.; He, L.; Ding, Y.; Gao, F.; et al. One-Pot Hydrothermal Synthesis of Magnetic N-Doped Sludge Biochar for Efficient Removal of Tetracycline from Various Environmental Waters. *Sep. Purif. Technol.* **2022**, *297*, 121426. [CrossRef]
51. Gugulothu, S.; Singh, S.A.; Madras, G. Superior Adsorption Capacity of Strontium Titanate and Titania Composites for Anionic Dyes Removal. *J. Environ. Chem. Eng.* **2017**, *5*, 4663–4675. [CrossRef]
52. Ali, I.; Asim, M.; Khan, T.A. Low Cost Adsorbents for the Removal of Organic Pollutants from Wastewater. *J. Environ. Manag.* **2012**, *113*, 170–183. [CrossRef] [PubMed]

53. Khan, T.A.; Chaudhry, S.A.; Ali, I. Equilibrium Uptake, Isotherm and Kinetic Studies of Cd(II) Adsorption onto Iron Oxide Activated Red Mud from Aqueous Solution. *J. Mol. Liq.* **2015**, *202*, 165–175. [CrossRef]
54. Rouhani, M.; Davoud, S.; Taghavi, K.; Naimi, M.; Jaafari, J. Evaluation of Tetracycline Removal by Adsorption Method Using Magnetic Iron Oxide Nanoparticles (Fe_3O_4) and Clinoptilolite from Aqueous Solutions. *J. Mol. Liq.* **2022**, *356*, 119040. [CrossRef]
55. Herath, I.; Kumarathilaka, P.; Al-Wabel, M.I.; Abduljabbar, A.; Ahmad, M.; Usman, A.R.A.; Vithanage, M. Mechanistic Modeling of Glyphosate Interaction with Rice Husk Derived Engineered Biochar. *Microporous Mesoporous Mater.* **2016**, *225*, 280–288. [CrossRef]
56. Ma, J.; Zhou, B.; Zhang, H.; Zhang, W.; Wang, Z. Activated Municipal Wasted Sludge Biochar Supported by Nanoscale Fe/Cu Composites for Tetracycline Removal from Water. *Chem. Eng. Res. Des.* **2019**, *149*, 209–219. [CrossRef]
57. Chen, Z.; Mu, D.; Chen, F.; Tan, N. $NiFe_2O_4$@Nitrogen-Doped Carbon Hollow Spheres with Highly Efficient and Recyclable Adsorption of Tetracycline. *RSC Adv.* **2019**, *9*, 10445–10453. [CrossRef]
58. Jannat Abadi, M.H.; Nouri, S.M.M.; Zhiani, R.; Heydarzadeh, H.D.; Motavalizadehkakhky, A. Removal of Tetracycline from Aqueous Solution Using Fe-Doped Zeolite. *Int. J. Ind. Chem.* **2019**, *10*, 291–300. [CrossRef]
59. Dai, J.; Meng, X.; Zhang, Y.; Huang, Y. Effects of Modification and Magnetization of Rice Straw Derived Biochar on Adsorption of Tetracycline from Water. *Bioresour. Technol.* **2020**, *311*, 123455. [CrossRef]
60. Zhang, Z.; Lan, H.; Liu, H.; Qu, J. Removal of Tetracycline Antibiotics from Aqueous Solution by Amino-Fe (III) Functionalized SBA15. *Colloids Surfaces A Physicochem. Eng. Asp.* **2015**, *471*, 133–138. [CrossRef]
61. Sun, S.; Jiang, Q.; Zhang, W.; Tian, L.; Li, T.; Zheng, L.; Gao, Y.; Zeng, X.; Zhou, L. Efficient Adsorption of Tetracycline in Aquatic System by Thermally-Treated Sediment. *Environ. Res.* **2022**, *214*, 113779. [CrossRef] [PubMed]
62. Croitoru, C.; Roata, I.C.; Pascu, A.; Stanciu, E.M. Diffusion and Controlled Release in Physically Crosslinked Poly (Vinyl Alcohol)/Iota-Carrageenan Hydrogel Blends. *Polymers* **2020**, *12*, 1544. [CrossRef] [PubMed]
63. Dai, Y.; Li, J.; Shan, D. Adsorption of Tetracycline in Aqueous Solution by Biochar Derived from Waste Auricularia Auricula Dregs. *Chemosphere* **2020**, *238*, 124432. [CrossRef] [PubMed]
64. Liu, H.; Xu, G.; Li, G. The Characteristics of Pharmaceutical Sludge-Derived Biochar and Its Application for the Adsorption of Tetracycline. *Sci. Total Environ.* **2020**, *747*, 141492. [CrossRef] [PubMed]
65. Chen, Y.; Wang, F.; Duan, L.; Yang, H.; Gao, J. Tetracycline Adsorption onto Rice Husk Ash, an Agricultural Waste: Its Kinetic and Thermodynamic Studies. *J. Mol. Liq.* **2016**, *222*, 487–494. [CrossRef]
66. Zhu, H.; Chen, T.; Liu, J.; Li, D. Adsorption of Tetracycline Antibiotics from an Aqueous Solution onto Graphene Oxide/Calcium Alginate Composite Fibers. *RSC Adv.* **2018**, *8*, 2616–2621. [CrossRef]
67. Saood, M.; Alshabib, M.; Alam, U.; Nawaz, M.; Dalhat, N.; Meili, L.; Zubair, M. Comparative Adsorption of Eriochrome Black T onto Recyclable Steel Dust Wastes: Isotherm, Kinetics and Thermodynamic Studies. *Colloids Surf. A Physicochem. Eng. Asp.* **2022**, *645*, 128828. [CrossRef]
68. Shao, N.; Tang, S.; Liu, Z.; Li, L.; Yan, F.; Liu, F.; Li, S.; Zhang, Z. Hierarchically Structured Calcium Silicate Hydrate-Based Nanocomposites Derived from Steel Slag for Highly Efficient Heavy Metal Removal from Wastewater. *ACS Sustain. Chem. Eng.* **2018**, *6*, 14926–14935. [CrossRef]
69. Lmz, Y.Z.; Zhang, S.; Wang, J.K.; Smith, R.W. Phosphorus Removal Using Steel Slag. *Acta Metall. Sin.* **2006**, *19*, 449–454.